LETTER

doi:10.1038/nature14102

EFF-1-mediated regenerative axonal fusion requires components of the apoptotic pathway

Brent Neumann[1], Sean Coakley[1]*, Rosina Giordano-Santini[1]*, Casey Linton[1], Eui Seung Lee[2], Akihisa Nakagawa[2], Ding Xue[2] & Massimo A. Hilliard[1]

Functional regeneration after nervous system injury requires transected axons to reconnect with their original target tissue. Axonal fusion, a spontaneous regenerative mechanism identified in several species, provides an efficient means of achieving target reconnection as a regrowing axon is able to contact and fuse with its own separated axon fragment, thereby re-establishing the original axonal tract[1–7]. Here we report a molecular characterization of this process in *Caenorhabditis elegans*, revealing dynamic changes in the subcellular localization of the EFF-1 fusogen after axotomy, and establishing phosphatidylserine (PS) and the PS receptor (PSR-1) as critical components for axonal fusion. PSR-1 functions cell-autonomously in the regrowing neuron and, instead of acting in its canonical signalling pathway[8], acts in a parallel phagocytic pathway that includes the transthyretin protein TTR-52, as well as CED-7, NRF-5 and CED-6 (refs 9–12). We show that TTR-52 binds to PS exposed on the injured axon, and can restore fusion several hours after injury. We propose that PS functions as a 'save-me' signal for the distal fragment, allowing conserved apoptotic cell clearance molecules to function in re-establishing axonal integrity during regeneration of the nervous system.

Axonal fusion, which occurs spontaneously in several invertebrate species[1–7], is a highly efficient means to re-establish the connection between an injured neuron and its target tissue; the proximal axon which is still attached to the cell body regrows towards, reconnects, and fuses with its separated distal fragment. We and others have shown that axonal fusion occurs in *C. elegans* mechanosensory neurons[4,7]. However, the genetic components of this process remain largely unidentified, with the nematode-specific fusogen, epithelial fusion failure 1 (EFF-1), the only protein known to be involved[4].

We expressed green fluorescent protein (GFP) specifically within the six mechanosensory neurons of *C. elegans* (Fig. 1a) and performed laser axotomy of the posterior lateral mechanosensory (PLM) neurons. We then analysed severed axons that re-established a contact between the regrowing proximal axon and its separated distal fragment (Extended Data Fig. 1); maintenance, or inhibition of degeneration of the distal axonal fragment, was used as evidence of successful fusion, whereas degeneration indicated unsuccessful fusion[7]. In wild-type animals, 80% of axons that displayed proximal–distal reconnection underwent successful fusion (Fig. 1b, d). EFF-1, a trimeric fusogen similar to class-II viral fusion proteins[13,14], mediates a wide range of fusion events in *C. elegans*[15,16], including the sculpting of dendritic arbors through self-fusion of excessive branches[17]. Animals lacking EFF-1 displayed a strong defect in axonal fusion[4] (Fig. 1c, d). To determine where EFF-1 is required, we expressed a GFP-tagged version of this protein specifically in the mechanosensory neurons. This transgene could rescue the axonal fusion defect of *eff-1* null animals, indicating a cell-autonomous function of EFF-1 in PLM (Fig. 1d). Prior to axotomy, we observed EFF-1::GFP in an indiscriminate punctate pattern throughout the PLM cell body and axon (Fig. 1e and Extended Data Fig. 2a). Soon after axotomy, a 'cap' of EFF-1::GFP appeared on the membrane at the tips of both the proximal and distal segments by the cut site (Extended Data Fig. 2b, c). Following regenerative growth, we consistently observed EFF-1::GFP on the membrane of the growth cone (Fig. 1f and Extended Data Figs 2d and 3a, b), suggesting rapid re-localization of EFF-1 to mediate fusion once contact is re-established.

We speculated that axonal fusion might share similarities with apoptotic cell corpse clearance, in which plasma membrane phospholipid asymmetry is lost. PS, normally restricted to the cytoplasmic leaflet, becomes externalized to the exoplasmic leaflet of the apoptotic cell, which enables its recognition by phagocytic cells[18]. Two different loss-of-function deletions in the PS receptor gene *psr-1* (refs 8 and 19) caused a strong reduction in axonal fusion (Fig. 2a, b). Furthermore, double mutants between *eff-1* and *psr-1* were no more defective than *eff-1* mutants (Fig. 2b), indicating that *psr-1* and *eff-1* are in the same genetic pathway. PSR-1 contains two highly conserved functional domains, an extracellular lysine-rich PS binding domain[20], and an intracellular JmjC domain with multiple enzymatic activities[21–23]. We expressed different versions of full-length *psr-1* cDNA selectively in the mechanosensory neurons of *psr-1* mutant animals. Expression of wild-type cDNA rescued axonal fusion (Fig. 2c), demonstrating that PSR-1 functions cell-autonomously within PLM. Next, we expressed *psr-1* cDNA carrying mutations that disrupt either its PS binding activity (K308E/K315E)[20] or its Fe(II) binding site (H192A/D194A) in the JmjC domain[20] and found that they no longer rescued the axonal fusion defect (Fig. 2c). Thus, PSR-1 requires both the extracellular PS binding domain and the intracellular JmjC domain for its cell-autonomous activity in axonal fusion.

To determine where PSR-1 functions within PLM, we analysed the localization of a functional mCherry-tagged version of PSR-1 in this neuron (Fig. 2c). PSR-1 localized to the nucleus and mitochondria of PLM (Fig. 2d and Extended Data Fig. 4a, b). However, following axotomy, we observed an accumulation of PSR-1::mCherry towards the end of the regrowing proximal axon (Fig. 2d and Extended Data Fig. 4b). Thus, PSR-1 is normally confined to the nucleus and mitochondria of PLM, but may be re-localized following injury.

PSR-1 functions in a signalling pathway that includes CED-2/CrkII, CED-5/Dock180, CED-12/ELMO and CED-10/RAC1 to mediate the recognition and removal of apoptotic cells[8,24–26] (Fig. 3a). We found that other components of this engulfment pathway are not required for axonal fusion, as animals carrying mutations in *ced-2*, *ced-5*, *ced-12*, or *ced-10* were not defective (Extended Data Fig. 5a). Similarly, the core apoptotic pathway is not required, as mutations in CED-9/BCL-2, CED-4/APAF-1, or cell-killing caspase *ced-3* did not significantly alter axonal fusion (Supplementary Table 1). Next, we analysed components of another, partly redundant cell corpse engulfment pathway, which includes the secreted PS binding protein TTR-52/transthyretin[10], the lipid-binding protein NRF-5 (ref. 12), the membrane-bound CED-7/ABC transporter[11], the transmembrane receptor CED-1/LRP1/MEGF10 (ref. 27), and the intracellular adaptor CED-6/GULP[9] (Fig. 3a). We found that TTR-52 was critical for successful axonal fusion (Fig. 3b and Extended Data Fig. 5b).

[1]CJCADR, Queensland Brain Institute, The University of Queensland, Brisbane QLD 4072, Australia. [2]Department of Molecular, Cellular, and Developmental Biology, University of Colorado, Boulder, Colorado 80309, USA.

*These authors contributed equally to this work.

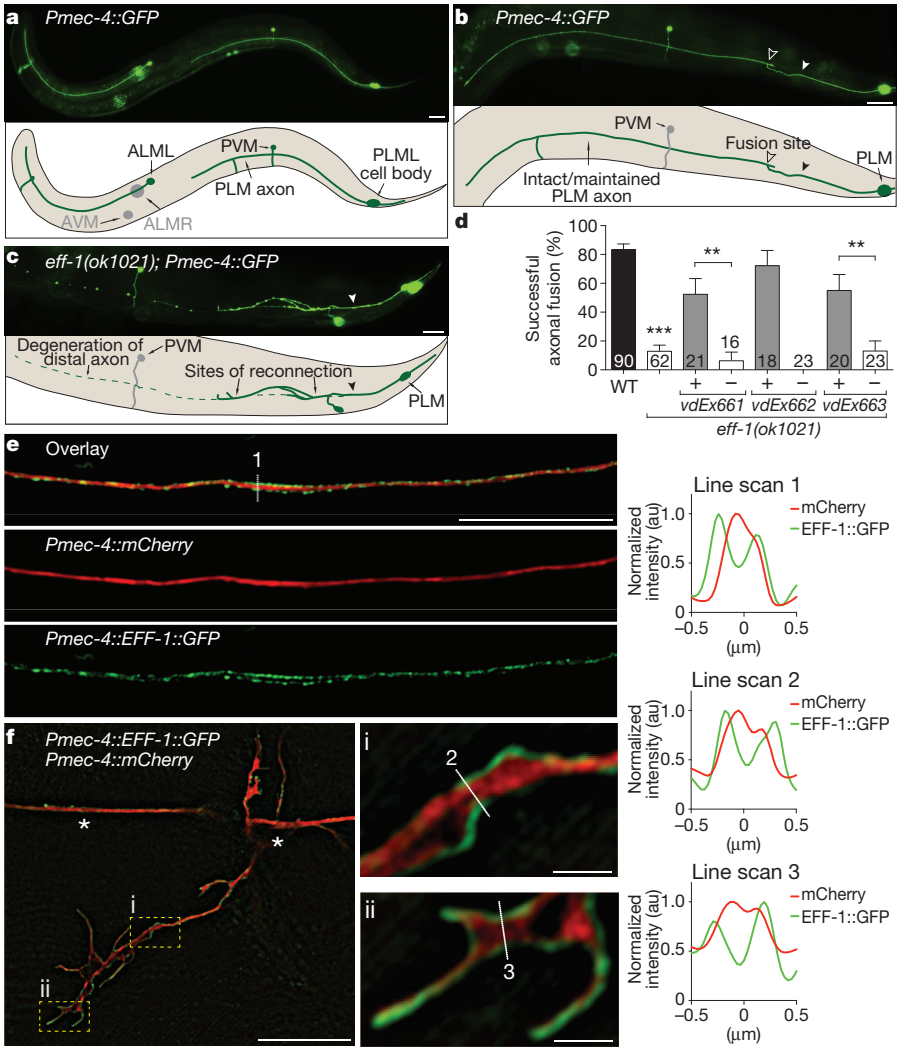

Figure 1 | EFF-1 mediates axonal fusion cell-autonomously and localizes to the membrane of growth cones. **a**, A wild-type (WT) *zdIs5(Pmec-4::GFP)* animal with fluorescent mechanosensory neurons. Anterior is left and ventral is down in this and all following images. Out of focus neurons are shown in grey in the schematic. Scale bar, 25 µm. Image representative of 242 animals. **b**, Successful axonal fusion in a WT animal, 24 h post-axotomy. Filled arrowhead points to the cut site; open arrowheads point to the fusion site. Scale bar, 25 µm. Image representative of 75 animals. **c**, Defective axonal fusion in an *eff-1(ok1021)* mutant animal 48 h post-axotomy. Filled arrowhead points to the cut site. Scale bar, 25 µm. Image representative of 54 animals. **d**, Quantification of axonal fusion in *eff-1(ok1021)* animals compared to WT, and cell-autonomous rescue with expression of *Pmec-4::EFF-1::GFP* in independent transgenic lines. Error bars indicate standard error of proportion. *n* values listed adjacent to each bar. *P* values from *t*-test: $^{**}P < 0.01$, $^{***}P < 0.001$ compared to WT, unless marked on graph. **e**, Single-plane structured illumination microscopy image of an intact axon carrying the transgene *vdEx662(Pmec-4::EFF-1::GFP; Pmec-4::mCherry)* in an *eff-1(ok1021)* mutant background. Fluorescence profiles from line scan 1 illustrate the presence of EFF-1::GFP on a section of the axonal membrane. Scale bar, 10 µm. au, arbitrary units. Images representative of 15 animals. **f**, Single-plane structured illumination microscopy image 18 h post-axotomy (left and middle panels). Right panels, fluorescence profiles from line scans 2 and 3 (taken from middle panels) illustrate the presence of EFF-1::GFP on the membrane of the growth cone. Asterisks show out of focus sections. Scale bars, 10 µm (left panel), 1 µm (middle panels). Images representative of 3 animals.

As TTR-52 is normally secreted from intestinal cells to bind PS exposed by apoptotic cells[10], we asked whether TTR-52 binding to PS also occurred after axonal injury. TTR-52 tagged with mCherry and expressed from a heat-shock promoter rescued the axonal fusion defect when induced either at the time of injury, or up to 6 h after injury (Fig. 3b and Extended Data Fig. 5c–g). We then used the same functional transgene to visualize TTR-52 before and after PLM axotomy. Following axotomy, TTR-52 rapidly localized to both the distal and proximal axon segments, with slightly stronger mCherry signals observed on the distal segment (Fig. 3d, e). These results suggest that TTR-52 functions as a secreted molecule that binds injured axonal fragments to mediate their regenerative fusion. To further confirm that TTR-52 was binding PS, we analysed the localization of a secreted version of Annexin V (sAnxV), a highly efficient and specific calcium-dependent PS binding protein[28]. PS was rapidly exposed on the proximal and distal PLM axon segments following axotomy, with the sAnxV::mRFP signal strongest on the distal segment (Fig. 3f and Extended Data Fig. 5h). This localization pattern closely matched that of TTR-52::mCherry (Fig. 3d, e), supporting a model in which PS is exposed on the axonal membrane after injury and acts as a 'save-me' signal for TTR-52 binding, thereby triggering reconnection and fusion.

Next we examined the involvement of the other components of the TTR-52 engulfment pathway. Inactivation of *ced-1* caused a modest defect, whereas animals lacking NRF-5, CED-7, or CED-6 displayed strong fusion defects (Fig. 3c and Supplementary Table 1). Double mutants between *psr-1* and either *ttr-52*, *ced-1*, *nrf-5*, *ced-7* or *ced-6* were no more defective than single mutant animals (Fig. 3c and Supplementary Table 1), indicating that PSR-1 functions within this TTR-52-mediated pathway during axonal fusion. Similar to *psr-1; eff-1* double mutant animals (Fig. 2b), double mutants between *eff-1* and either *ttr-52*, *ced-1*,

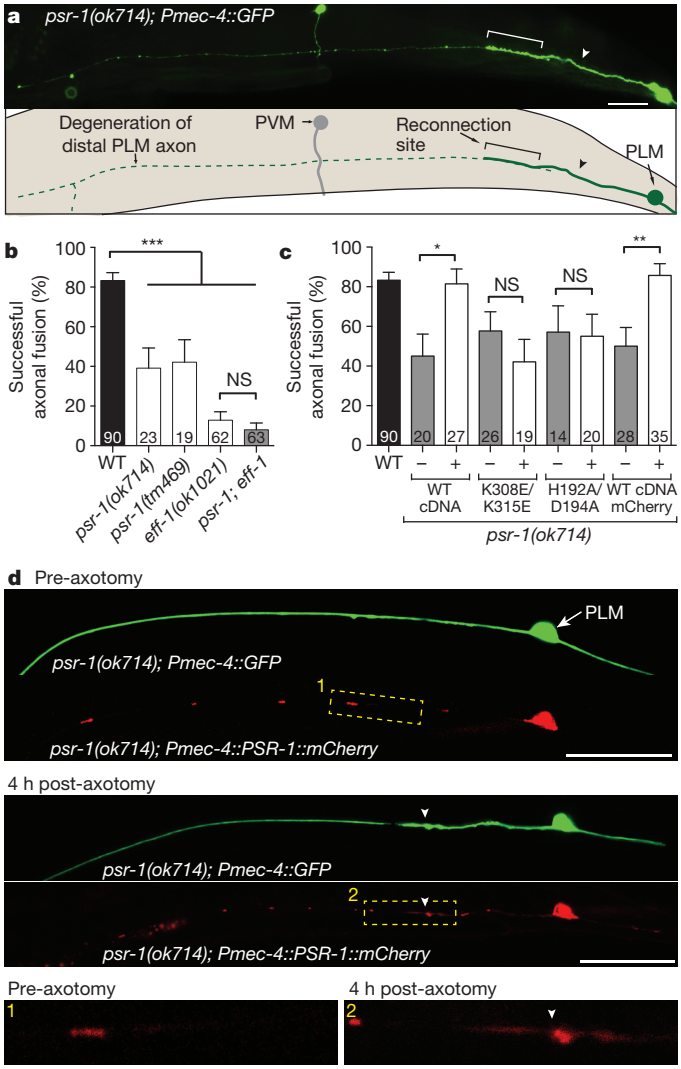

Figure 2 | PSR-1 functions cell-autonomously in regulating axonal fusion. **a**, Unsuccessful fusion in a *psr-1(ok714)* mutant animal 24 h after axotomy. Bracket highlights the region of reconnection. Scale bar, 25 μm. Image representative of 14 animals. **b**, Quantification of successful fusion events in wild-type (WT, black bar), and single (white bars) and double (grey bar) mutant animals. **c**, Cell-autonomous rescue in *psr-1(ok714)* animals with expression of WT *psr-1* cDNA (untagged or tagged with mCherry) in the mechanosensory neurons. Expression of *psr-1* cDNA carrying mutations in the PS binding (K308E/K315E), or in the JmjC domain (H192A/D194A), fails to rescue the defect; representative results from the six independent lines tested. For **b** and **c**, error bars indicate standard error of proportion. *n* values within each bar. *P* values from *t*-test: $*P < 0.05$, $**P < 0.01$, $***P < 0.001$ compared to WT unless marked on graph. NS, not significant. **d**, Single plane confocal images showing the localization of PSR-1::mCherry in PLM in a *psr-1(ok714)* mutant animal before axotomy (top two panels), and 4 h post-axotomy (middle two panels). Bottom panels show magnified images of boxed regions to highlight accumulation of PSR-1 at the end of the regrowing proximal axon. Arrowheads point to cut site. Scale bar, 25 μm. Image representative of 21 animals.

ced-6 or *ced-7* were no more defective than single *eff-1* mutants (Extended Data Fig. 3c), indicating that these genes act in the same genetic pathway. Importantly, overexpression of EFF-1 specifically in the mechanosensory neurons could overcome the axonal fusion defects caused by mutation of either *psr-1* or *ttr-52* (Extended Data Fig. 3d), demonstrating that EFF-1 functions genetically downstream of these molecules. Notably, although mutations in some axonal fusion genes caused defective PLM regrowth, we found no correlation between regrowth and axonal fusion (Extended Data Fig. 6 and Supplementary Table 2).

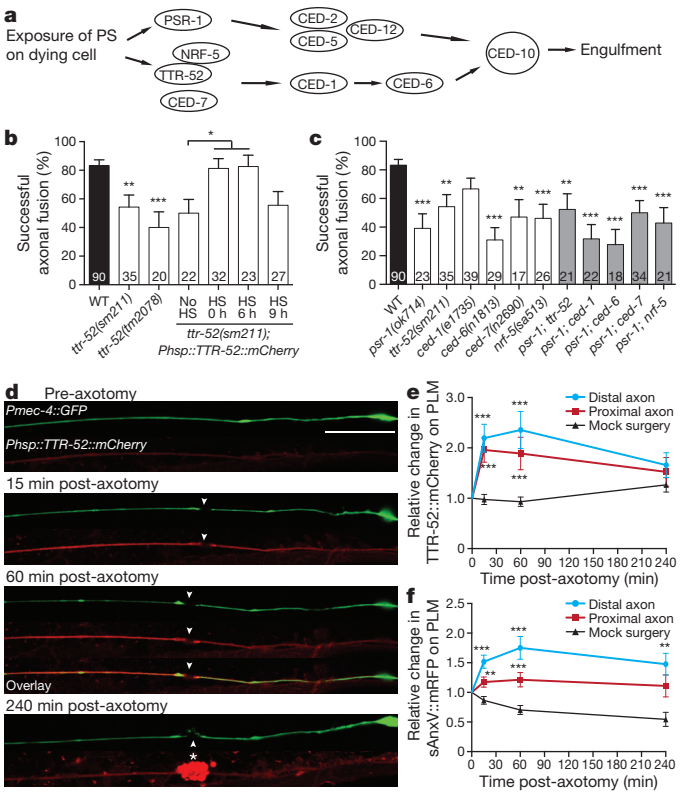

Figure 3 | PSR-1 functions in the TTR-52 pathway during axonal fusion. **a**, Schematic of two partially redundant parallel pathways that mediate recognition and engulfment of apoptotic cells. **b**, TTR-52 is required for successful axonal fusion. Expression of TTR-52::mCherry rescues the defect when induced from a heat-shock (HS) promoter immediately after axotomy (0 h) and up to 6 h post-axotomy. **c**, Mutations in genes acting in the *ttr-52* pathway reduce axonal fusion, and double mutants with *psr-1* are not more defective than single mutants. For **b** and **c**, error bars indicate standard error of proportion. *n* values within each bar; *P* values from *t*-test: $*P < 0.05$, $**P < 0.01$, $***P < 0.001$. **d**, Single plane confocal images showing the localization of TTR-52::mCherry in *ttr-52(sm211)* mutants to the PLM axon before axotomy and at several time points after transection. Filled arrowheads point to cut sites, asterisk highlights accumulation of TTR-52::mCherry at the injury site. Scale bar, 25 μm. Image representative of 22 animals. **e**, **f**, Quantification of the relative fluorescence levels of TTR-52::mCherry (**e**) and sAnxV::mRFP (**f**) on the distal and proximal PLM axonal segments after transection compared to mock surgery conditions. Error bars indicate standard error. *n* values for distal and proximal $n = 22$ (**e**) and $n = 26$ (**f**), for mock surgery $n = 23$ (**e**) and $n = 21$ (**f**). *P* values from Kolmogorov–Smirnov test: $**P < 0.01$, $***P < 0.001$ compared to mock surgery.

Similar to the localization pattern of PSR-1, we observed that a functional tagged version of CED-6 (mRFP::CED-6) predominantly localized to mitochondria in PLM, and accumulated in the regrowing proximal segment after axotomy (Extended Data Fig. 7a–c). Next, we analysed localization of a tagged version of the ABC transporter, CED-7 (CED-7::mRFP), which could cell-autonomously rescue the axonal fusion defect (Extended Data Fig. 7a), and found a diffuse localization pattern throughout the PLM axon before, and at several time points after axotomy (Extended Data Fig. 7d). Finally, we analysed the localization of NRF-5, a lipid-binding molecule that is normally secreted from the body wall muscle cells during apoptotic clearance[12]. Using a mCherry-tagged version of NRF-5 expressed from a heat-shock promoter, we found that NRF-5 binds to the PLM axon after axotomy (Extended Data Fig. 7e, f). This suggests that, similarly to TTR-52, NRF-5 may recognize and bind to the exposed PS signal following injury.

We have previously shown that, although axonal fusion is a highly specific process, non-specific fusion can occur when a second axon in close proximity to PLM is also severed[7]. The PLN axon fasciculates with

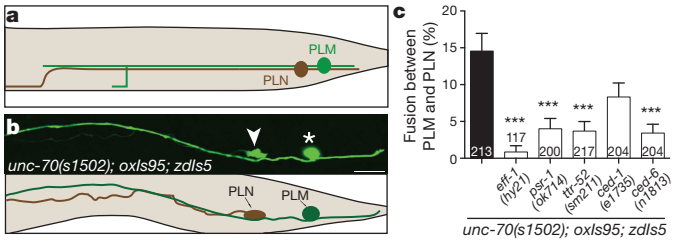

Figure 4 | Apoptotic molecules mediate non-specific axonal fusion caused by mutation of *unc-70*. **a**, Schematic showing fasciculation between the axons of PLN (brown) and PLM (green). **b**, Loss of *unc-70* causes spontaneous fusion between PLM (asterisk) and PLN (arrowhead) (appearance of GFP in PLN); single plane confocal image is shown. Scale bar, 10 μm. Image representative of 31 animals. **c**, The frequency of non-specific fusion events is strongly reduced in animals with mutations in *eff-1*, *psr-1, ttr-52* and *ced-6*. Error bars indicate standard error of proportion. *n* values shown adjacent to each bar. *P* values from *t*-test: $***P < 0.001$ compared to *unc-70(s1502)*.

that of PLM (Fig. 4a), and when both axons are simultaneously transected approximately 10% of animals undergo non-specific fusion between these two neurons[7]. We observed a similar phenotype in animals deficient in UNC-70/β-spectrin, a genetic background in which the axons of *C. elegans* motor neurons undergo spontaneous cycles of breaks followed by regeneration[29]. We observed that *unc-70* mutant animals display aberrant PLM axonal morphology comprising breaks, loop structures, and branching (Extended Data Fig. 8a, b), as well as transfer of fluorophores between PLM and PLN (Fig. 4b, c). Time-lapse imaging and a tethered-fluorophore assay demonstrated that this transfer of fluorophores occurred through fusion events, and was not due to aberrant promoter activity (Extended Data Fig. 8c, d). These fusion events were dependent on the EFF-1 fusogen and required DLK-1, a mitogen-activated triple kinase essential for regeneration[30] (Fig. 4c and Extended Data Fig. 8e). Remarkably, we found that loss of *psr-1*, *ttr-52,* or *ced-6* caused a strong reduction in *unc-70*-induced PLM–PLN fusion (Fig. 4c). Analogous to our finding post-axotomy, we observed TTR-52::mCherry and sAnxV::mRFP binding to the PLM axon in *unc-70* mutants (Extended Data Fig. 9), suggesting that axonal damage induced by this genetic insult could also trigger the flipping of PS to the external surface of the membrane.

Thus, recognition of separated distal segments by a regrowing axon is achieved by changes in lipid membrane composition, and is mediated by apoptotic clearance molecules with the fusogen EFF-1 acting downstream to restore membrane and cytoplasmic continuity (Extended Data Fig. 10 and Supplementary Discussion).

Online Content Methods, along with any additional Extended Data display items and Source Data, are available in the online version of the paper; references unique to these sections appear only in the online paper.

Received 13 December 2013; accepted 19 November 2014.

1. Bedi, S. S. & Glanzman, D. L. Axonal rejoining inhibits injury-induced long-term changes in *Aplysia* sensory neurons *in vitro*. *J. Neurosci.* **21,** 9667–9677 (2001).
2. Birse, S. C. & Bittner, G. D. Regeneration of giant axons in earthworms. *Brain Res.* **113,** 575–581 (1976).
3. Deriemer, S. A., Elliott, E. J., Macagno, E. R. & Muller, K. J. Morphological evidence that regenerating axons can fuse with severed axon segments. *Brain Res.* **272,** 157–161 (1983).
4. Ghosh-Roy, A., Wu, Z., Goncharov, A., Jin, Y. & Chisholm, A. D. Calcium and cyclic AMP promote axonal regeneration in *Caenorhabditis elegans* and require DLK-1 kinase. *J. Neurosci.* **30,** 3175–3183 (2010).
5. Hoy, R. R., Bittner, G. D. & Kennedy, D. Regeneration in crustacean motoneurons: evidence for axonal fusion. *Science* **156,** 251–252 (1967).
6. Macagno, E. R., Muller, K. J. & DeRiemer, S. A. Regeneration of axons and synaptic connections by touch sensory neurons in the leech central nervous system. *J. Neurosci.* **5,** 2510–2521 (1985).
7. Neumann, B., Nguyen, K. C., Hall, D. H., Ben-Yakar, A. & Hilliard, M. A. Axonal regeneration proceeds through specific axonal fusion in transected *C. elegans* neurons. *Dev. Dyn.* **240,** 1365–1372 (2011).
8. Wang, X. *et al.* Cell corpse engulfment mediated by *C. elegans* phosphatidylserine receptor through CED-5 and CED-12. *Science* **302,** 1563–1566 (2003).
9. Liu, Q. A. & Hengartner, M. O. Candidate adaptor protein CED-6 promotes the engulfment of apoptotic cells in *C. elegans*. *Cell* **93,** 961–972 (1998).
10. Wang, X. *et al. Caenorhabditis elegans* transthyretin-like protein TTR-52 mediates recognition of apoptotic cells by the CED-1 phagocyte receptor. *Nature Cell Biol.* **12,** 655–664 (2010).
11. Wu, Y. C. & Horvitz, H. R. The *C. elegans* cell corpse engulfment gene *ced-7* encodes a protein similar to ABC transporters. *Cell* **93,** 951–960 (1998).
12. Zhang, Y., Wang, H., Kage-Nakadai, E., Mitani, S. & Wang, X. *C. elegans* secreted lipid-binding protein NRF-5 mediates PS appearance on phagocytes for cell corpse engulfment. *Curr. Biol.* **22,** 1276–1284 (2012).
13. Pérez-Vargas, J. *et al.* Structural basis of eukaryotic cell–cell fusion. *Cell* **157,** 407–419 (2014).
14. Zeev-Ben-Mordehai, T., Vasishtan, D., Siebert, C. A. & Grunewald, K. The full-length cell–cell fusogen EFF-1 is monomeric and upright on the membrane. *Nat. Commun.* **5,** 3912 (2014).
15. Mohler, W. A. *et al.* The type I membrane protein EFF-1 is essential for developmental cell fusion. *Dev. Cell* **2,** 355–362 (2002).
16. Podbilewicz, B. Cell fusion. *WormBook* http://dx.doi.org/10.1895/wormbook.1.52.1 (2006).
17. Oren-Suissa, M., Hall, D. H., Treinin, M., Shemer, G. & Podbilewicz, B. The fusogen EFF-1 controls sculpting of mechanosensory dendrites. *Science* **328,** 1285–1288 (2010).
18. Fadok, V. A. *et al.* Exposure of phosphatidylserine on the surface of apoptotic lymphocytes triggers specific recognition and removal by macrophages. *J. Immunol.* **148,** 2207–2216 (1992).
19. Fadok, V. A. *et al.* A receptor for phosphatidylserine-specific clearance of apoptotic cells. *Nature* **405,** 85–90 (2000).
20. Yang, H. *et al.* A lysine-rich motif in the phosphatidylserine receptor PSR-1 mediates recognition and removal of apoptotic cells. *Nat. Commun.* http://dx.doi.org/10.1038/ncomms6717 (in the press).
21. Chang, B., Chen, Y., Zhao, Y. & Bruick, R. K. JMJD6 is a histone arginine demethylase. *Science* **318,** 444–447 (2007).
22. Hong, X. *et al.* Interaction of JMJD6 with single-stranded RNA. *Proc. Natl Acad. Sci. USA* **107,** 14568–14572 (2010).
23. Webby, C. J. *et al.* Jmjd6 catalyses lysyl-hydroxylation of U2AF65, a protein associated with RNA splicing. *Science* **325,** 90–93 (2009).
24. Gumienny, T. L. *et al.* CED-12/ELMO, a novel member of the CrkII/Dock180/Rac pathway, is required for phagocytosis and cell migration. *Cell* **107,** 27–41 (2001).
25. Reddien, P. W. & Horvitz, H. R. CED-2/CrkII and CED-10/Rac control phagocytosis and cell migration in *Caenorhabditis elegans*. *Nature Cell Biol.* **2,** 131–136 (2000).
26. Wu, Y. C. & Horvitz, H. R. *C. elegans* phagocytosis and cell-migration protein CED-5 is similar to human DOCK180. *Nature* **392,** 501–504 (1998).
27. Zhou, Z., Hartwieg, E. & Horvitz, H. R. CED-1 is a transmembrane receptor that mediates cell corpse engulfment in *C. elegans*. *Cell* **104,** 43–56 (2001).
28. Mapes, J. *et al.* CED-1, CED-7, and TTR-52 regulate surface phosphatidylserine expression on apoptotic and phagocytic cells. *Curr. Biol.* **22,** 1267–1275 (2012).
29. Hammarlund, M., Jorgensen, E. M. & Bastiani, M. J. Axons break in animals lacking β-spectrin. *J. Cell Biol.* **176,** 269–275 (2007).
30. Hammarlund, M., Nix, P., Hauth, L., Jorgensen, E. M. & Bastiani, M. Axon regeneration requires a conserved MAP kinase pathway. *Science* **323,** 802–806 (2009).

Supplementary Information is available in the online version of the paper.

Acknowledgements We thank L. Hammond and S. Roy for support with microscopy; R. Tweedale for comments on the manuscript; P. Bazzicalupo, D. Hall, K. Nguyen, and members of the Hilliard laboratory for discussions and comments; and E. Jorgensen, S. Shaham and X. Wang for sharing reagents. Some strains were provided by the CGC, which is funded by NIH Office of Research Infrastructure Programs (P40 OD010440), and the International *C. elegans* Gene Knockout Consortium. This work was supported by NHMRC Project Grants 631634 and 1068871, NIH R01 NS060129, and ARC Future Fellowship FT110100097 to M.A.H.; NIH grants GM059083, GM079097 and GM088241 to D.X.; HFSPO Fellowship LT000762/2012 to R.G.S.; Australian Postgraduate Award to S.C.; The University of Queensland Research Scholarship to C.L.; and ARC LIEF grant LE130100078 for microscopy.

Author Contributions B.N., S.C., and R.G.S. carried out most experiments. C.L., E.S.L., and A.N. contributed some experiments. D.X. provided reagents, designed PSR-1 experiments, and edited the paper. B.N. and M.A.H. designed and interpreted experiments and wrote the paper.

Author Information Reprints and permissions information is available at www.nature.com/reprints. The authors declare no competing financial interests. Readers are welcome to comment on the online version of the paper. Correspondence and requests for materials should be addressed to M.A.H. (m.hilliard@uq.edu.au).

METHODS

Strains and genetics. Standard techniques were used for *C. elegans* maintenance, crosses and other genetic manipulations[31]. All experiments were performed on hermaphrodites grown at room temperature (~22 °C) unless otherwise stated, and all strains were grown on OP50 bacteria, except for animals carrying the *unc-70(s1502)* mutation, which were grown on HB101 bacteria. The following mutations were used: LGI: *ced-1(e1735)*, *ced-12(bz187)*, *dlk-1(ju476)*, *sem-4(n1971)*; LGII: *eff-1(ok1021)*, *eff-1(hy21)*; LGIII: *ced-4(n1162)*, *ced-6(n1813)*, *ced-7(n2690)*, *ced-9(n1950)*, *ttr-52(sm211)*, *ttr-52(tm2078)*; LGIV: *ced-2(e1752)*, *ced-3(n717)*, *ced-5(n1812)*, *ced-10 (n3246)*, *psr-1(ok714)*, *psr-1(tm469)*; LGV: *nrf-5(sa513)*, *unc-70(s1502)*. The transgenes used were: *smIs119[Phsp16-2::ttr-52::mCherry]*[10], *smIs95[Phsp16-2::sAnxV::mRFP]*[32], *oxIs95[Ppdi-2::unc-70; Pmyo2::GFP]*[29], *qxIs92[Phsp::nrf-5::mCherry]* (a gift from Xiaochen Wang), *vdEx575[Pmec-4::psr-1(c)* (10 ng μl^{-1}), *Podr-1::DsRed* (30 ng μl^{-1})*]*, *vdEx661/vdEx662/vdEx663[Pmec-4::EFF-1::GFP* (5 ng μl^{-1}); *Pmec-4::mCherry* (20 ng μl^{-1}); *Podr-1::DsRed* (60 ng μl^{-1})*]*, *vdEx705[Pmec-4::psr-1(c) (H192A/D194A)* (10 ng μl^{-1}); *Podr-1::DsRed* (30 ng μl^{-1})*]*, *vdEx709[Pmec-4::psr-1(c)(K308E/K315E)* (10 ng μl^{-1}); *Podr-1::DsRed* (30 ng μl^{-1})*]*, *vdEx851[Pmec-4::eff-1* (5 ng μl^{-1}); *Podr-1::DsRed* (60 ng μl^{-1})*]*, *vdEx862[Pmec-4::psr-1(c)::mCherry* (2.5 ng μl^{-1}); *Podr-1::DsRed* (25 ng μl^{-1})*]*, *vdEx876[Pmec-4::tomm-20::GFP* (0.5 ng μl^{-1}); *Podr-1::GFP* (50 ng μl^{-1})*]*, *vdEx895[Pmec-4::mRFP::ced-6* (5 ng μl^{-1}); *Podr-1::DsRed* (30 ng μl^{-1})*]*, *vdEx998[Pmec-4::ced-7::mRFP* (2.5 ng μl^{-1}); *Podr-1::DsRed* (30 ng μl^{-1})*]*, *zdIs5[Pmec-4::GFP]*.

Molecular biology. Standard molecular biology techniques were used. The *Pmec-4::EFF-1* plasmid was created by excising *EFF-1* from a *Podr-1::EFF-1* plasmid using Kpn I and Apa I restriction enzymes, and cloning it in front of the *Pmec-4* promoter in a *Pmec-4::unc-54_3′* UTR plasmid. To build the *Pmec-4::EFF-1::GFP* plasmid, *eff-1* genomic DNA was amplified (fwd primer 5′-ctagctagcatggaaccgccgtttgagtg-3′; rev primer 5′-gaaccggtttaatgtactggctactgctatag-3′) and cloned into the pSM-mCherry plasmid using Nhe I and Age I restriction enzymes, to obtain *pSM::EFF-1::mCherry*. The *mec-4* promoter was then cloned from plasmid *pSM::Pmec-4::EFF-1* into *pSM::EFF-1::mCherry* using Sal I and Sph I restriction enzymes, to obtain *Pmec-4::EFF-1::mCherry*. Finally, an Age I/Apa I fragment from plasmid *pCP.179* (ref. 33) (a gift from Shai Shaham) was cloned into *Pmec-4::EFF-1::mCherry* to obtain *Pmec-4::EFF-1::GFP*. The *Pmec-4::psr-1(c)* plasmid was generated through insertion of a Bam HI/Age I *psr-1* cDNA amplicon between the *mec-4* promoter and the *unc-54* 3′UTR. The following primers were used: fwd primer 5′-tcagtgggatccatgtcattagggcgagatag-3′; rev primer 5′-tcagtgaccggtttaaac tagcgagttctgaaaat-3′. The *Pmec-4::psr-1(c)::mCherry* plasmid was created in similar fashion, except a different reverse primer was used (rev primer 5′-tcagtgaccggtc gaactagcgagttctgaaaataag-3′) and the cDNA was cloned into a *Pmec-4::mCherry::unc-54_3′UTR* plasmid. QuikChange mutagenesis (Agilent Technologies, Santa Clara, CA) was used to introduce the K308/K315E and H192A/D194A mutations, with the *Pmec-4::psr-1(c)* plasmid used as the template. The *ced-6* gene was amplified from genomic DNA and inserted downstream of mRFP into a *Pmec-4::mRFP::unc-54_3′UTR* plasmid using Xma I and Age I restriction enzymes. The following primers were used: fwd primer 5′-tcagtccccgggaatggcaaaagacatttacaa gacc-3′; rev primer 5′-tcagtcaccggtttattgcttcaaattcatcattttcg-3′. The *Pmec-4::tomm-20::GFP* plasmid was created by switching the mRFP fluorophore from a *Pmec-4::tomm-20::mRFP*[34] plasmid using Age I and Eco RI restriction enzymes. *Pmec-4::ced-7::mRFP* was created through insertion of full-length *ced-7* cDNA upstream of the mRFP sequence in a *Pmec-4::mRFP::unc-54_3′UTR* plasmid using Xma I and Nhe I restriction enzymes and the following primers: fwd primer 5′-tcagtgcccgg gatgaatagattgcgacaattctc-3′, and rev primer 5′-tcagtggctagcgacatgtgtggaatgggaaa tc-3′.

Laser axotomy and microscopy. Animals were immobilized in 0.05% tetramisole hydrochloride on 4% agar pads. Axotomies were performed as previously described[7], using a MicroPoint Laser System Basic Unit attached to a Zeiss Axio Imager A1 (Objective EC Plan-Neofluar 100×/1.30 Oil M27). Axons were severed in L4 or one-day-old adult (for localization of TTR-52, sAnxV, and NRF-5) animals approximately 50 μm anterior to the PLM cell body, visualized on a Zeiss Axio Imager Z1 microscope equipped with a Photometrics camera (Cool Snap HQ2; Tucson, AZ) and analysed with MetaMorph software (Molecular Devices, Sunnyvale, CA) or ImageJ 1.48s. Animals were analysed 24 h post-axotomy for regrowth, reconnection and fusion. Regrowth was recorded as the length of regenerative growth from the proximal side of the cut site: the proximal axon was traced from the start of regrowth to the tip of the longest regenerative branch using Metamorph software; neurons that underwent axonal fusion were excluded from these quantifications. Axons were deemed to be reconnected when the proximal and distal axons were visually connected and within the same focal plane when observed with a 63× objective (Extended Data Fig. 1). Axonal fusion was defined as proximal–distal reconnection that prevented the onset of degeneration in the distal axon[7]. For clarification of successful fusion, animals were re-analysed at 48 h and/or 72 h post-axotomy as necessary.

To analyse a selection of reconnection events with greater resolution, three-dimensional structured illumination microscopy (3D-SIM) was performed with an Elyra PS.1 SIM/STORM microscope, using a 63× 1.4 NA oil objective. To visualize reconnection sites, *z*-stacks (3D-SIM) were acquired and SIM processing performed. Green fluorescence was visualized with a 488 nm laser (10% power, 50 ms exposure time, 28 μm grating, 3 rotations). Processing was completed with a sectioning of 100/83/83. Wild-type and *eff-1(ok1021)* mutant animals were analysed 24 h post-axotomy and scored for proximal–distal reconnection with both standard compound imaging and 3D-SIM. Reconnection was scored separately and double blinded with respect to each technique before comparisons were made to determine the accuracy between the two techniques. In cases where the distal fragment had become too faint, SIM processing could not be completed.

Visualization of EFF-1. To study the localization of EFF-1::GFP in regrowing axons, laser axotomies were performed in animals carrying the *vdEx662* transgene in 0.05% tetramisole. Acquisitions were performed on animals mounted on 10% agarose pads in M9, in 25 mM sodium azide. Individual animals were then imaged 30 min, 3 h, 8 h and 18–24 h after axotomy using a LSM 710 META confocal microscope, equipped with a GaAsP detector and Zen 2012 software. Green fluorescence was visualized with a 488 nm laser (10% power, with a gain of 600 and 4× averaging) and red fluorescence was visualized with a 543 nm laser (1.4% power, with a gain of 500 and 4× averaging). Image analysis was performed using ImageJ 1.48s. To score for the presence of EFF-1::GFP on the membrane of regrowing axons, fluorescence profiles of line scans at different sections of the regrowing axon tip were obtained using the 'Plot Profile' tool in ImageJ. EFF-1::GFP was scored as localizing to the membrane if the peak of green intensity (EFF-1::GFP) and the peak of red intensity (cytoplasmic mCherry) were not overlapping.

To visualize EFF-1::GFP by SIM, axotomized animals were mounted in 10% agarose pads in M9, in 25 mM sodium azide. Single plane acquisitions (2D-SIM) were performed with an Elyra PS.1 SIM/STORM microscope, using a 63× 1.4 NA oil objective, and SIM processing was performed using the ZEN software 2012, Black edition. Green fluorescence was visualized with a 488 nm laser (20% power, 200–400 ms exposure time, 28 μm grating, 3 rotations) and red fluorescence was visualized with a 561 nm laser (10% power, 200 ms exposure time, 34 μm grating, 3 rotations). Processing was completed with a sectioning of 100/83/83. Fluorescence profiles of line scans were obtained as described above.

Visualization of other tagged proteins. The subcellular localization of PSR-1::mCherry, mRFP::CED-6, CED-7::mRFP, and NRF-5::mCherry was analysed in animals immobilized with 0.05% tetramisole with a LSM 710 META confocal microscope, equipped with a GaAsP detector and Zen 2012 software. Green cytoplasmic fluorescence was visualized with a 488 nm laser (0.15% power, with a gain of 650 and 4× averaging) and red fluorescence was visualized with a 561 nm laser (1.5% power, with a gain of 700 and 4× averaging for PSR-1 and CED-6; 0.7% power, with a gain of 600 and 4× averaging for CED-7; 2.4% power, with a gain of 700 and 8× averaging for NRF-5). TTR-52::mCherry and sAnxV::mRFP were visualized in one-day-old adult animals (unless stated otherwise) with a LSM 510 META confocal microscope and Zen 2008 software. Green fluorescence was analysed with a 488 nm laser (2.4% power, with a gain of 601 and 8× averaging) and red fluorescence with a 543 nm laser (100% power, with a gain of 1012 and 8× averaging).

Quantification of the binding of TTR-52, Annexin V, and NRF-5 to the PLM axon. Expression of transgenes was induced 4 h before analysis with incubation at 30 °C for 30 min. Changes in fluorescence intensity were calculated with line scans performed using ImageJ 1.46r software. To avoid bright fluorescence associated with collateral laser damage, line scans were recorded ~5 μm from the damage site on both the proximal and distal axon segments for a length of ~15 μm. Line scans were recorded along the same region for the 488 nm and 543 nm channels for each image. To control for changes in focus and intensity, mCherry/mRFP expression was normalized to GFP for each image and recorded relative to pre-axotomy levels. For the *unc-70* mutant background, analyses were performed as above, except that for TTR-52::mCherry line scans were recorded along the PLM axon for a length of ~15 μm, whereas for sAnxV::mRFP three separate line scans were recorded along the PLM axon for a length of ~5 μm, with the mean values used for each axon. Background fluorescence of the 488 nm and 543 nm channels was also subtracted from the corresponding axonal line scans.

Analysis of cell-cell fusion events in *unc-70* mutants. For time-lapse microscopy one-day-old adult *unc-70(s1502)* animals were immobilized in 0.05% tetramisole hydrochloride on 10% agar pads sealed with Vaseline and visualized using a Zeiss inverted spinning disk confocal microscope equipped with a Yokogawa W1 disk head and a Piezo *z*-drive. Images were acquired every 30 min for 15 h with a Hamamatsu Flash 4.0 scientific CMOS camera using Slidebook 5.0 software. Adult animals were used for the tethered fluorophore experiments, and the presence and location of TOMM-20::mRFP were scored in the PLM neuron, and GFP-positive PLN and additional neurons. For *unc-70(s1502)* animals, only those displaying PLM–PLN fusion were analysed.

Statistical analysis. Statistical analysis was performed using Primer of Biostatistics 3.01, GraphPad Prism and Microsoft Excel. Error of proportions was used to assess variation across a single population, two-way comparison was performed using the *t*-test, and ANOVA was used for more than two groups. For those data sets that did not follow a Normal distribution we used the Kolmogorov–Smirnov test (Fig. 3e, f and Extended Data Figs 5d–f, 6a, 7f, and 9c, f). No statistical method was used to predetermine sample size.

31. Brenner, S. The genetics of *Caenorhabditis elegans*. *Genetics* **77,** 71–94 (1974).
32. Zou, W. *et al. Caenorhabditis elegans* myotubularin MTM-1 negatively regulates the engulfment of apoptotic cells. *PLoS Genet.* **5,** e1000679 (2009).
33. Procko, C., Lu, Y. & Shaham, S. Glia delimit shape changes of sensory neuron receptive endings in *C. elegans*. *Development* **138,** 1371–1381 (2011).
34. Neumann, B. & Hilliard, M. A. Loss of MEC-17 leads to microtubule instability and axonal degeneration. *Cell Rep.* **6,** 93–103 (2014).
35. Mitani, S., Du, H., Hall, D. H., Driscoll, M. & Chalfie, M. Combinatorial control of touch receptor neuron expression in *Caenorhabditis elegans*. *Development* **119,** 773–783 (1993).

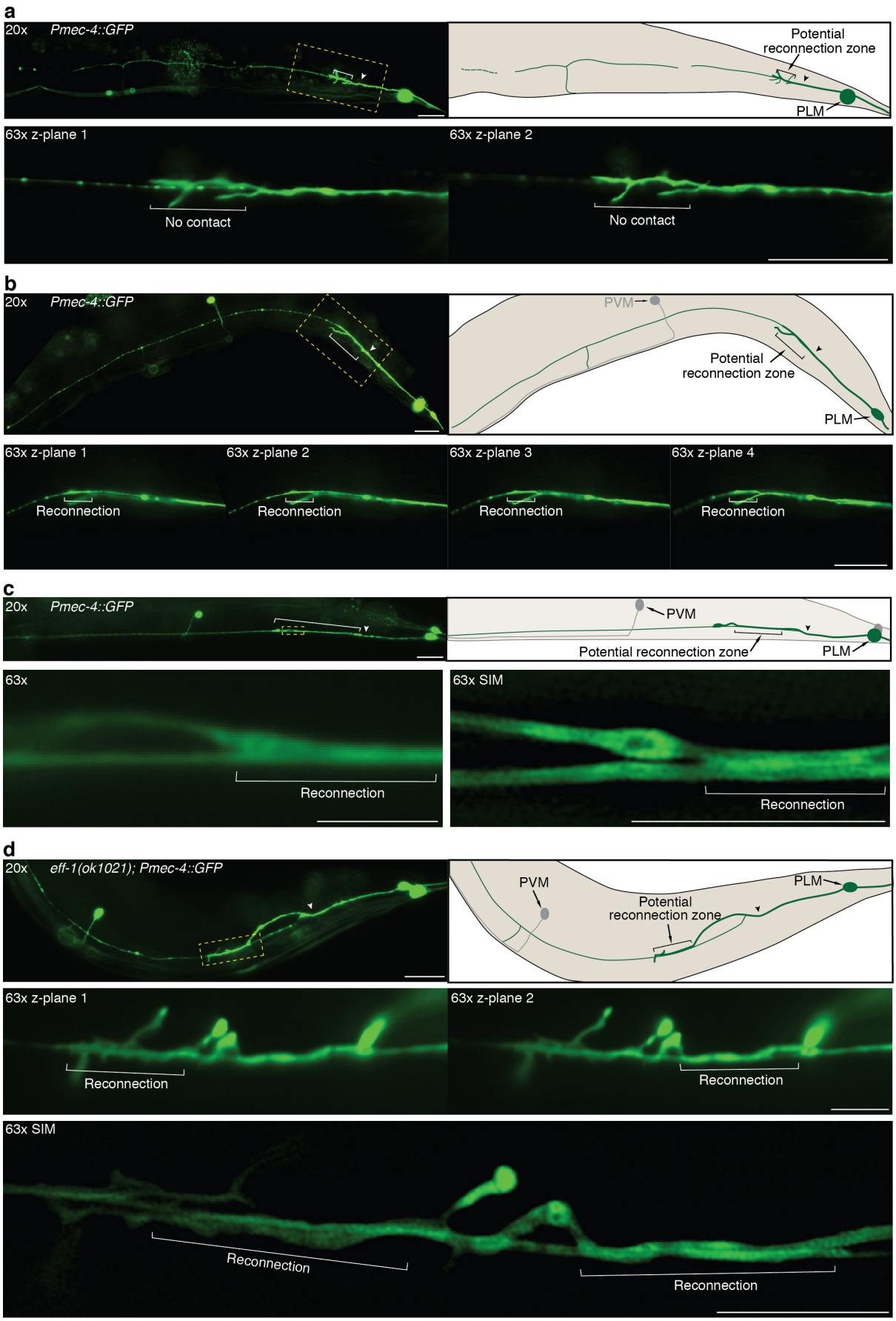

Extended Data Figure 1 | Analysis of proximal–distal reconnection using compound microscopy and 3D-SIM imaging. Typical examples of how reconnection was scored with compound microscopy (**a**, **b**). **a**, Image and schematic of a wild-type (WT) animal 24 h post-axotomy captured with a 20× objective (top panel) and two different *z* planes captured with a 63× objective. Despite visually appearing reconnected at 20×, the proximal regrowing axon has not made contact with the distal axon (63×); image representative of 150 animals. **b**, Representative images from a total of 90 animals taken with a 20× objective (top panels) and a 63× objective (bottom panels) of a WT animal 24 h post-axotomy in which reconnection has occurred between the proximal and distal axon segments. Three dimensional structured illumination microscopy (3D-SIM) was used to confirm contact regions between regrowing and distal axon fragments in WT (**c**) and *eff-1(ok1021)* mutant (**d**) animals. In each case that reconnection was observed with compound microscopy (63×), it was also evident with 3D-SIM imaging; $n = 14$ for each genotype. **c**, Successful reconnection in a WT animal, 24 h post-axotomy. Top panel: single-plane image acquired with a 20× objective on a compound microscope. Bottom panels: single-plane images acquired with a 63× objective on a compound microscope (left, 63×) and a SIM image of the same region (right, 63× SIM); images representative of 18 animals. **d**, Proximal–distal reconnection in an *eff-1(ok1021)* mutant animal, 24 h post-axotomy. Top panel: single-plane image acquired with a 20× objective on a compound microscope. Middle panel: single-plane images acquired with a 63× objective on a compound microscope (63×), showing two different *z*-planes where the regions indicated by brackets as 'contact' zones are in focus. Bottom panel: a SIM image of the same regions highlighting the points of contact; images representative of 14 animals. Arrowheads point to the site of axotomy, and brackets highlight zones of either potential (**a**) or actual reconnection (**b**–**d**). Dashed boxes represent regions magnified in the 63× images. Scale bars, 25 μm (**a**, **b** and 20× images in **c**, **d**) or 5 μm (63× images in **c**, **d**). Estimated resolution of SIM images (as per Zeiss software ZEN Black 2012): 120 nm in (**c**) and 110 nm in (**d**).

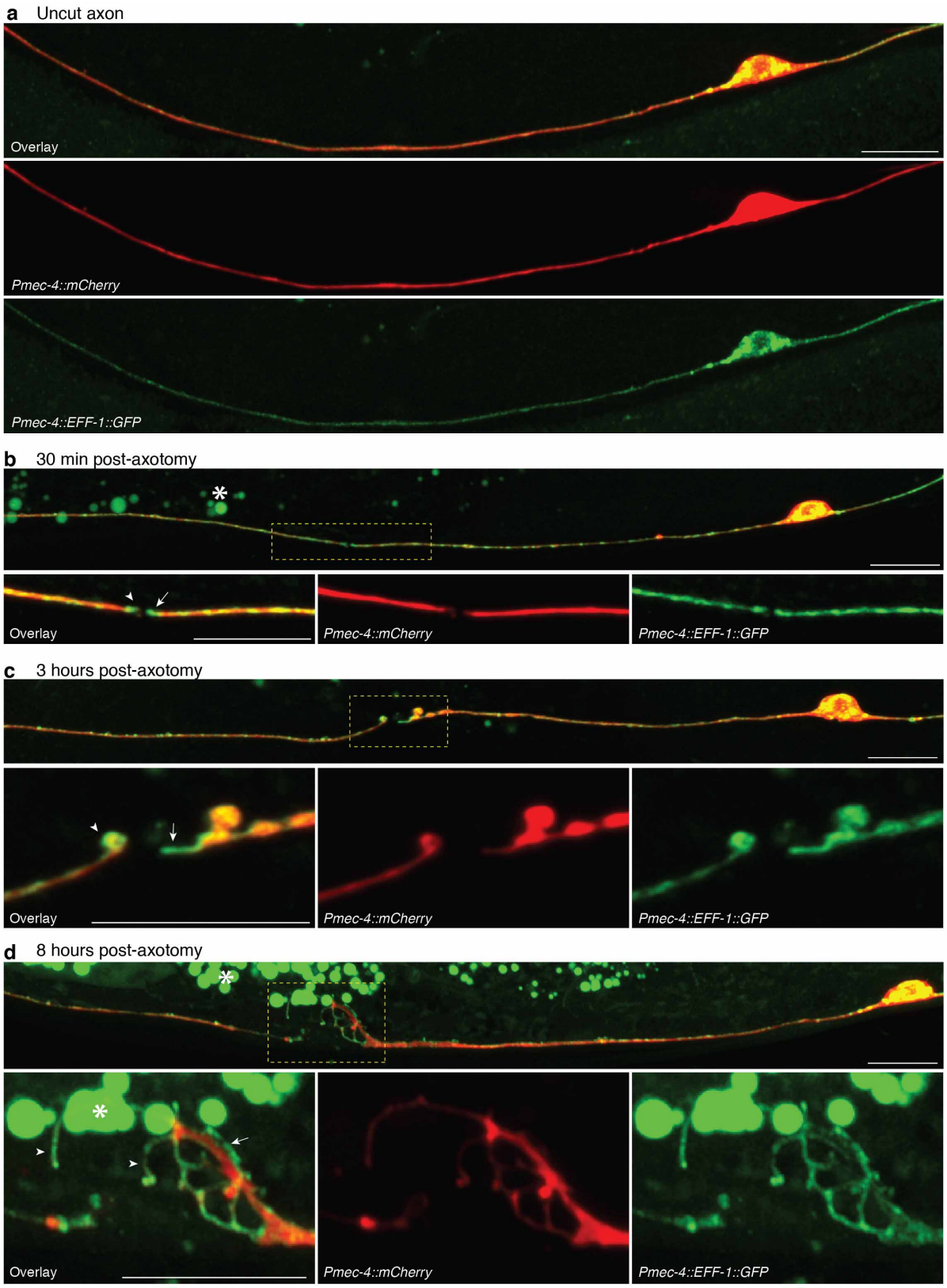

Extended Data Figure 2 | EFF-1 localization in PLM neurons before and after axotomy. Maximum projections of *z*-stack confocal images of an uncut axon and regrowing axons carrying the transgene *Pmec-4::EFF-1::GFP*; *Pmec-4::mCherry* in an *eff-1(ok1021)* mutant background. Representative images are shown for an intact axon (**a**), and axotomized axons 30 min post-axotomy (**b**), 3 h post-axotomy (**c**), and 8 h post-axotomy (**d**). **a**, In uncut axons, EFF-1 is present in the cell body (excluding the nucleus), posterior process and all along the axon in an irregular pattern. **b**, Thirty minutes after axotomy, EFF-1 forms a 'cap' on both the proximal (arrow) and distal (arrowhead) fragments. **c**, After 3 h, the proximal stump begins to swell. 'Capping' of the proximal (arrow) and distal (arrowhead) fragments by EFF-1 is still present. **d**, After 8 h, a growth cone with filopodia-like protrusions forms from the proximal stump. EFF-1 is present on the membrane of the growth cone (arrow) and filopodia-like structures (arrowheads). Scale bars, 10 μm. Asterisks highlight intestinal autofluorescence. Images representative of 15 (**a**), 12 (**b**), 9 (**c**), and 7 (**d**) animals.

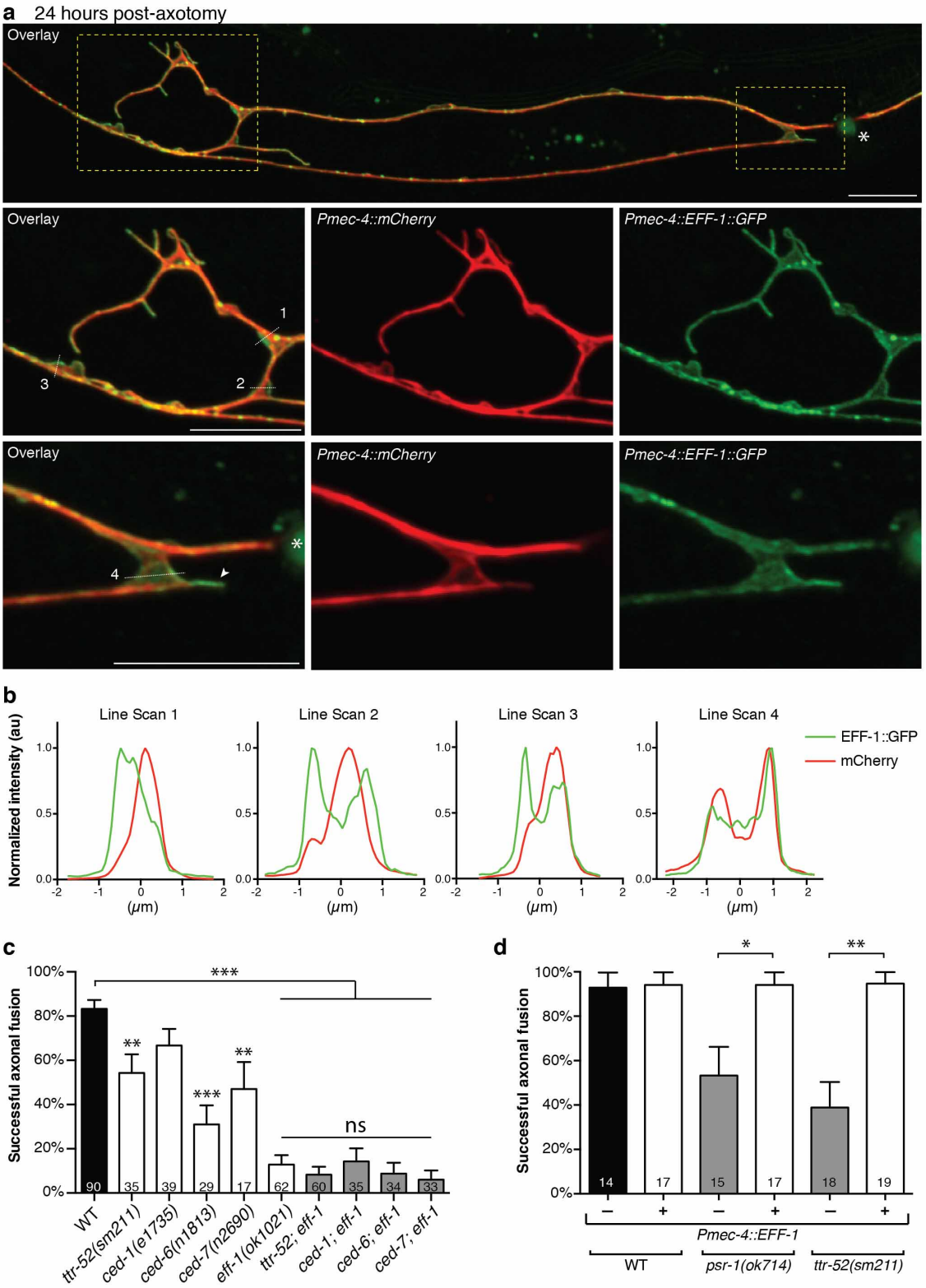

Extended Data Figure 3 | EFF-1 localizes to the membrane of growth cones, and functions genetically downstream from the apoptotic genes. **a**, Maximum projection of *z*-stack confocal images of a regrowing axon carrying the transgene *Pmec-4::EFF-1::GFP*; *Pmec-4::mCherry* in *eff-1(ok1021)* mutant background, 24 h post-axotomy. EFF-1 is present on the membrane of the growth cone (line scans 1, 2 and 3) and forms a 'cap' at the proximal tip of the distal fragment (arrowhead). Asterisk shows the scar at the cut site. Scale bars, 10 μm. Images representative of 8 animals. **b**, Fluorescence profiles from the line scans shown in the left panels of panel **a** illustrate the presence of EFF-1::GFP on the membrane of the growth cone (1 to 3) but not on the membrane of a putative fusion site (line scan 4). au, arbitrary units. **c**, Successful axonal fusion in single mutant animals (white bars) compared to double mutants with *eff-1(ok1021)* (grey bars). Double mutants do not show a worsening of the defect compared to *eff-1* single mutants. **d**, Cell-autonomous overexpression of EFF-1 (white bars) in wild-type (WT) animals, or in those carrying mutations in *psr-1* or *ttr-52*, rescuing their defect. For **c** and **d**, error bars represent standard error of proportion. *n* values shown adjacent to each bar. *P* values from *t*-test: $*P < 0.05$, $**P < 0.01$, $***P < 0.001$ compared to WT unless otherwise indicated. ns, not significant.

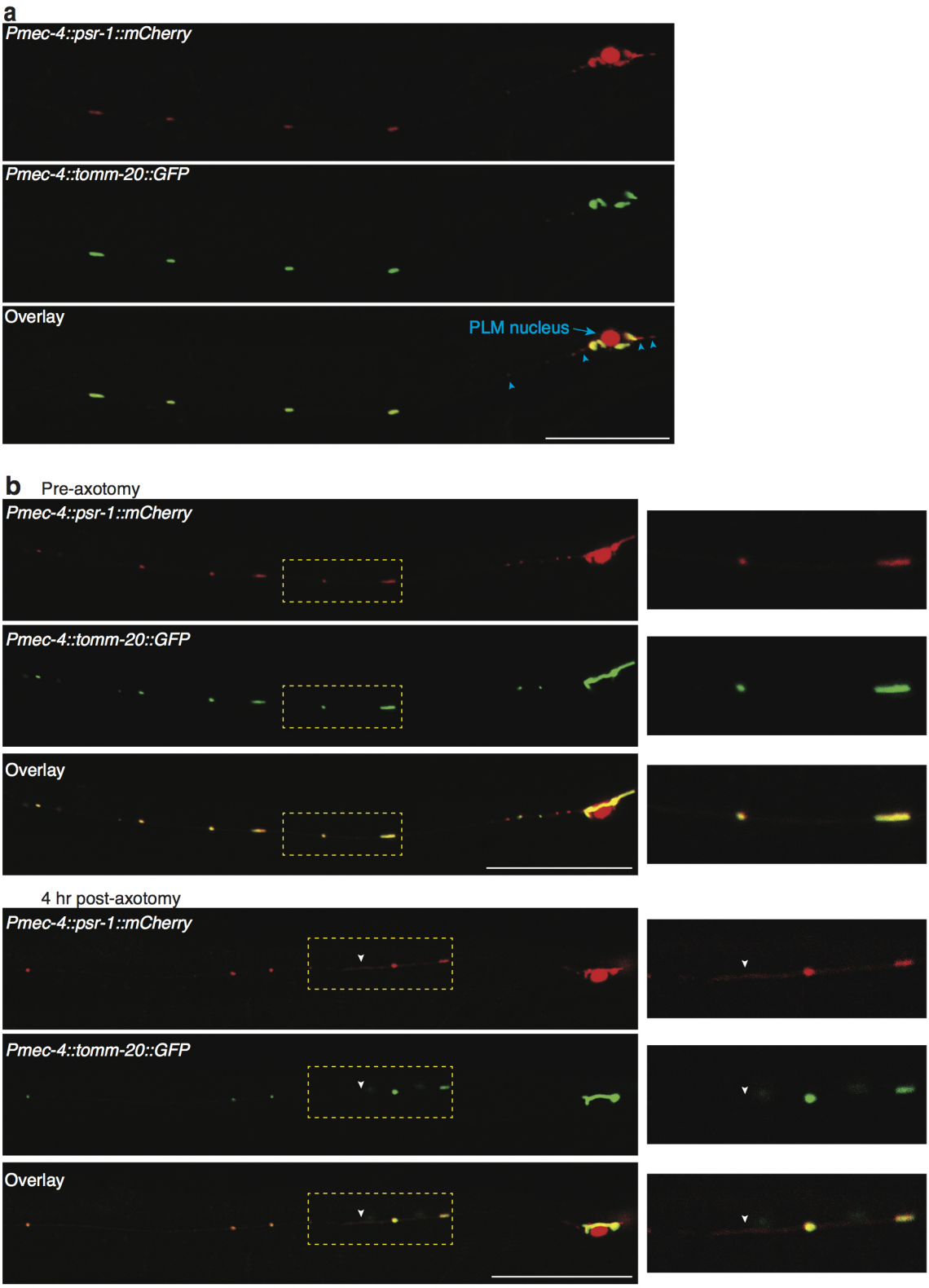

Extended Data Figure 4 | Analysis of the localization of functional fluorophore-tagged PSR-1. a, Maximum projection confocal images showing the co-localization of PSR-1::mCherry (top panel) with a mitochondrial marker (TOMM-20::GFP, middle panel) in a *psr-1(ok714)* mutant animal. PSR-1 displays strong co-localization with the mitochondria; however, there are regions where co-localization is not present, and these are highlighted by the arrow and arrowheads in the overlay image (bottom panel). Images are representative of 35 animals. Animals of the same genotype were analysed before and after axotomy (**b**) to determine the localization of PSR-1 compared to the mitochondrial marker during regrowth. PSR-1 accumulates to the end of the regrowing proximal axon, whereas the TOMM-20::GFP remains restricted to the mitochondria; images representative of 27 animals. Panels to the right show magnified views of the boxed regions; arrowheads point to the site of axotomy. Scale bars, 25 μm.

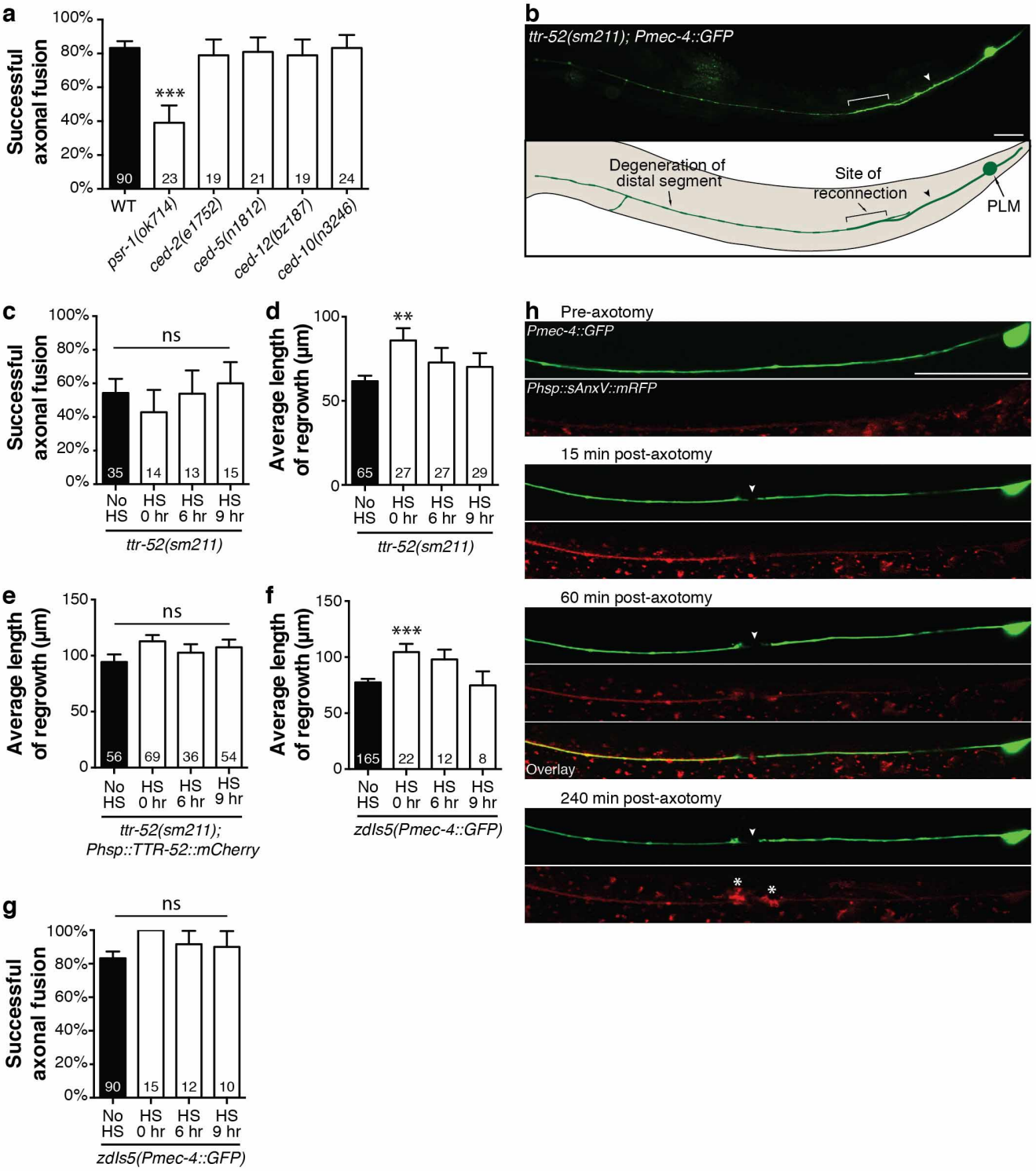

Extended Data Figure 5 | Analysis of axonal fusion and regeneration after heat-shock treatment in wild-type and *ttr-52* mutant animals, and analysis of sAnxV localization after axotomy. **a**, Animals mutant in *ced-2*, *ced-5*, *ced-12*, or *ced-10* have normal axonal fusion similar to that of wild-type (WT) animals. **b**, Unsuccessful fusion in a *ttr-52(sm211)* animal. Regrowth has extended from the cut site (arrowhead) and contacted the distal fragment (bracketed region), but degeneration of the distal fragment has begun. Scale bar, 25 µm. Image representative of 16 animals. **c**, Rate of successful axonal fusion in *ttr-52(sm211)* animals without or with heat-shock (HS) treatment. **d**, The average length of regrowth in *ttr-52(sm211)* animals given HS after axotomy compared to those without HS treatment. **e**, Quantification of regrowth in *ttr-52(sm211); Phsp::TTR-52::mCherry* animals without HS treatment compared to those that received HS immediately after axotomy (0 h), or at 6 or 9 h post-axotomy. **f**, Comparison of the average length of regrowth in *zdIs5* animals without HS or with HS given at different times after axotomy. **g**, Successful axonal fusion in *zdIs5* animals without HS compared to animals given HS at different times post-axotomy. Error bars represent standard error of proportion (**a**, **c**, **g**) and standard error (**d**–**f**). *n* values shown adjacent to each bar. *P* values (from *t*-test for **a**, **c**, **g**; from Kolmogorov–Smirnov test for **d**–**f**): $^{**}P < 0.01$, $^{***}P < 0.001$ compared to WT or no HS (black bars), unless marked otherwise on the graph. ns, not significant. **h**, Single plane confocal images showing the localization of the PS sensor, sAnxV::mRFP, to the axon of PLM before axotomy and at several time points after transection. The overlay image shows the 60 min time-point; filled arrowhead points to the site of axotomy, and asterisks highlight the accumulation of sAnxV::mRFP at the injury site. Scale bar, 25 µm. Images representative of 26 animals.

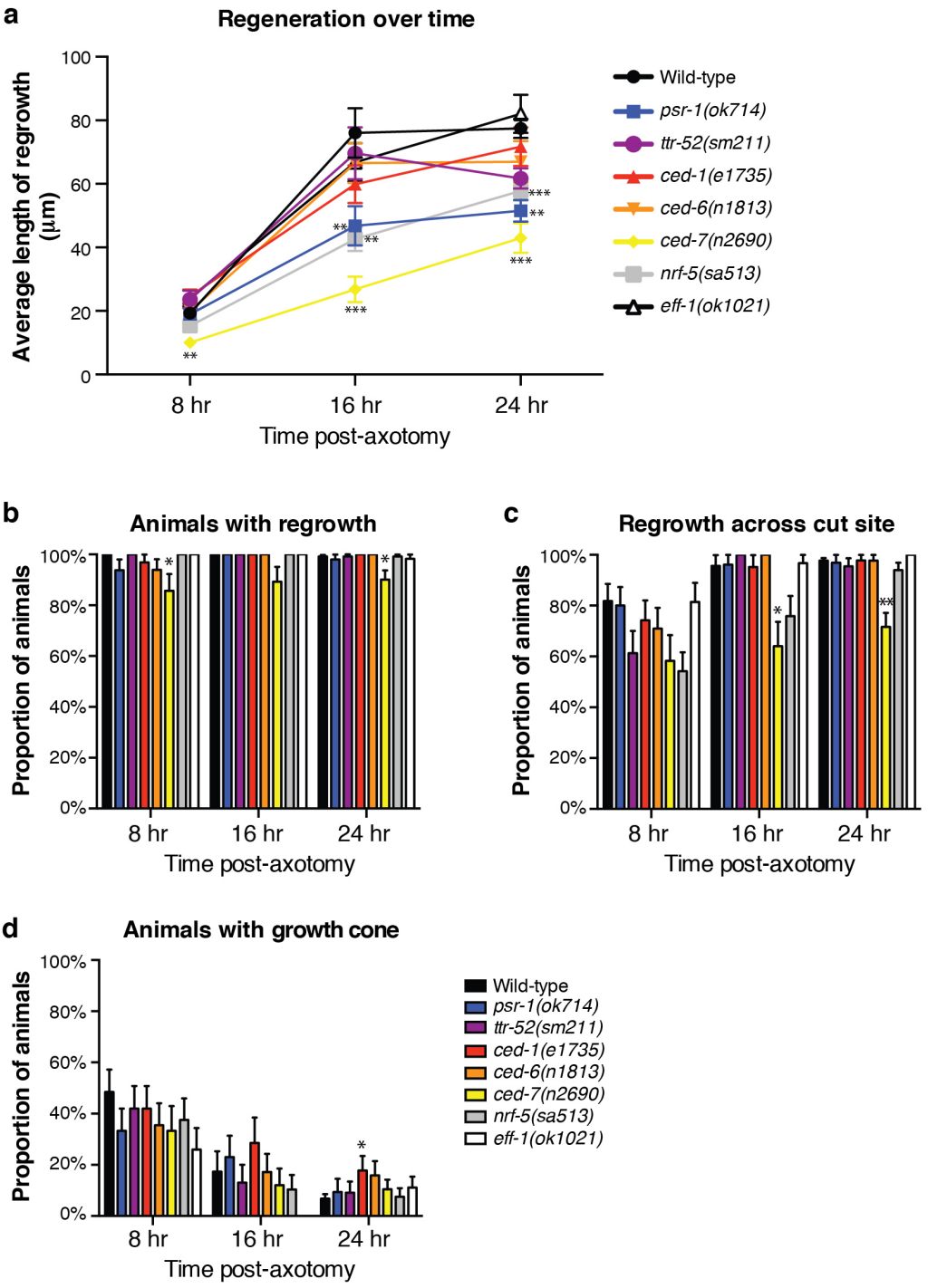

Extended Data Figure 6 | Quantification of regeneration. **a**, To determine if the loss of any of the genes analysed caused a reduction in the regenerative potential of PLM, we calculated the average length of regrowth over the first 24 h post-axotomy. Mutations in several genes that reduced axonal fusion, including *psr-1*, *ttr-52*, *nrf-5* and *ced-7*, caused defective regrowth in PLM. However, we found no correlation between the average length of regrowth and the rate of axonal fusion. For instance, *ced-10* and *ced-12* mutants displayed reduced regrowth (Supplementary Table 2), but presented no defect in axonal fusion (Extended Data Fig. 5a), whereas animals that lacked *eff-1* had the strongest defect in axonal fusion, but their regenerative growth was not different from that of wild-type (WT) animals. Moreover, there was no correlation between axonal fusion and the percentage of animals able to initiate any regrowth from the proximal axon after transection (**b**), the average number of axons that were able to regrow across the cut site at different time points after axotomy (**c**), or the percentage of axons presenting a growth cone at different stages of regeneration (**d**). Error bars represent standard error (**a**) or standard error of proportion (**b**–**d**). *n* values are displayed in Supplementary Table 2. *P* values (from Kolmogorov–Smirnov test for **a**; from *t*-test for **b**–**d**): $*P < 0.05$, $**P < 0.01$, $***P < 0.001$.

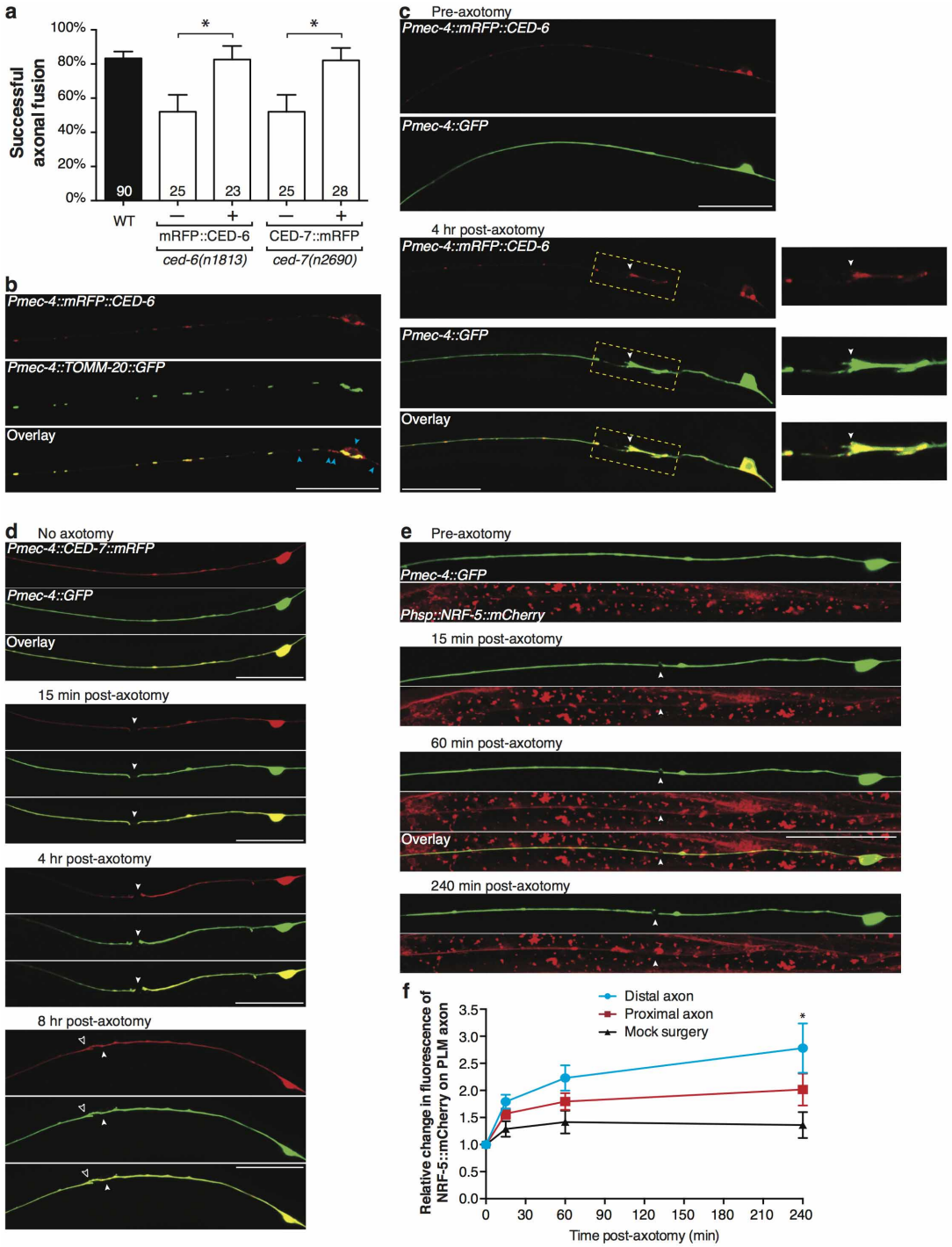

Extended Data Figure 7 | Localization of CED-6, CED-7, and NRF-5 in PLM before and after axotomy. **a**, Cell-autonomous rescue of the axonal fusion defect in *ced-6(n1813)* and *ced-7(n2690)* animals with expression in the mechanosensory neurons of either wild-type *ced-6* genomic DNA, or *ced-7* cDNA, tagged with mRFP. Error bars represent standard error of proportion; *n* values displayed in graph. *P* values from *t*-test: $*P < 0.05$. **b**, Maximum projection confocal images highlighting co-localization between mRFP::CED-6 and a mitochondrial marker (TOMM-20::GFP) in a *ced-6(n1813)* mutant background. Arrowheads point to regions where this co-localization is absent. Scale bar, 25 µm. Images representative of 12 animals. **c**, Single plane confocal images showing the localization of mRFP::CED-6 in PLM in a *ced-6(n1813)* mutant animal before axotomy (top two panels), and 4 h post-axotomy (bottom three panels). Panels to the right show magnified images of the boxed regions to highlight accumulation of CED-6 at the end of the regrowing proximal axon. Arrowheads point to the site of axotomy. Scale bars, 25 µm; images representative of 9 animals. **d**, CED-7::mRFP localization in single plane confocal images of PLM in *ced-7(n2690)* mutant animals without axotomy (top panels) and at several time points after axotomy. Different animals are shown for each time point. Filled arrowheads point to the site of axotomy; open arrowhead points to site of fusion. Scale bars, 25 µm. Images representative of 10 animals. **e**, Single plane confocal images of the localization of NRF-5::mCherry (expressed from a heat-shock promoter) in *nrf-5* mutants to the PLM axon before axotomy and at several time points after transection in animals with genotype *nrf-5(sa513); qxIs92; zdIs5*. Overlay image is shown for the 60 min time-point; arrowheads point to the site of axotomy. Scale bar, 25 µm. Images representative of 29 animals. **f**, Quantification of the relative fluorescence levels of NRF-5::mCherry on the PLM distal (blue line) and proximal (red line) axons after axotomy compared to mock surgery conditions (black line). Error bars represent standard error; $n = 29$ for distal and proximal axon, $n = 13$ for mock surgery. *P* values from Kolmogorov–Smirnov test: $*P < 0.05$ compared to mock surgery.

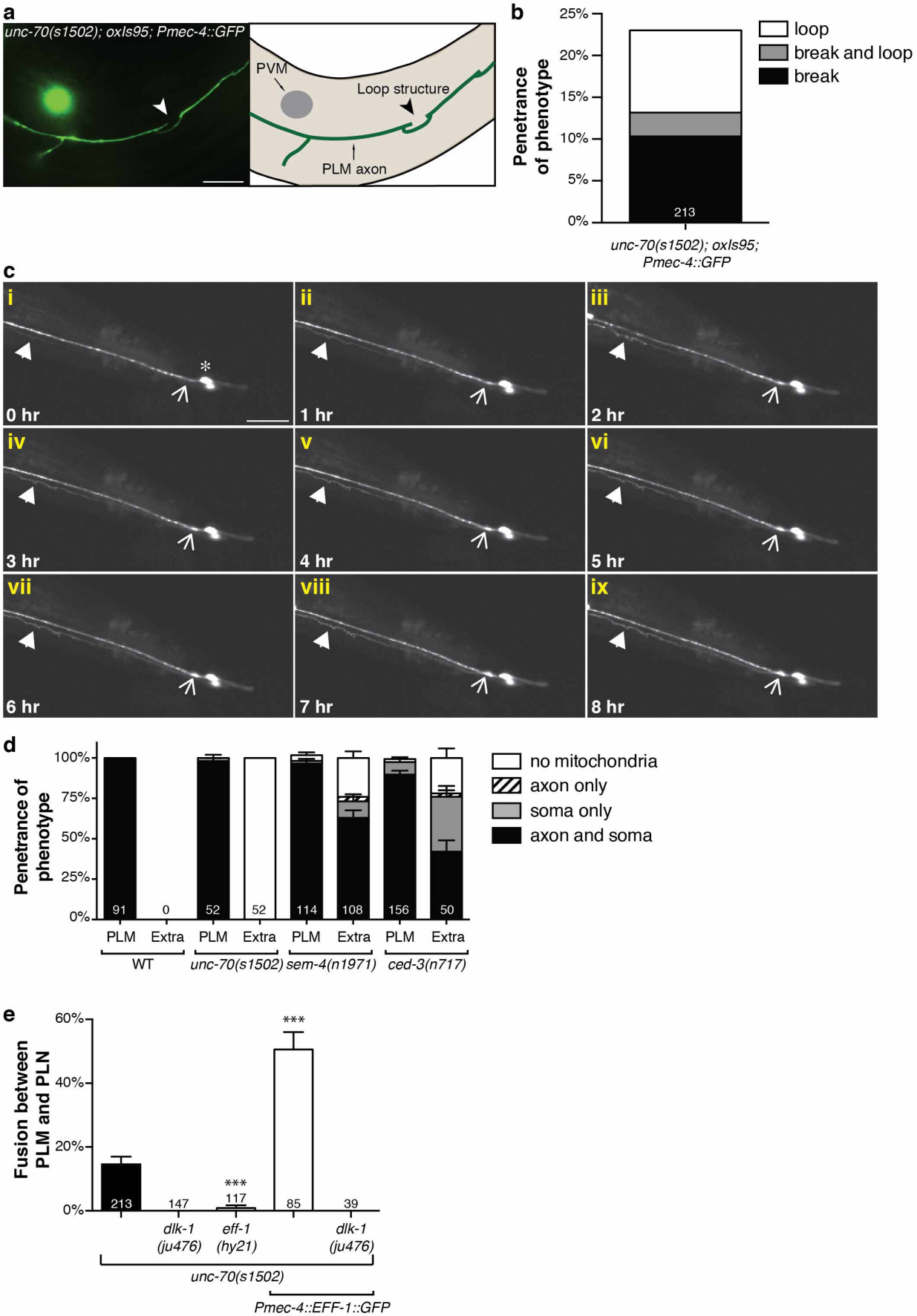

Extended Data Figure 8 | Mutation of *unc-70* causes axonal defects and PLM-PLN fusion events that are dependent on *eff-1* and *dlk-1*. **a**, In the absence of UNC-70 the PLM mechanosensory neurons develop abnormal morphology with breaks, loop structures (arrowhead) and branching. Scale bar, 25 μm; image representative of 21 animals. **b**, Quantification of the penetrance of abnormal loop structures as well as axonal breakages; *n* value within the bar. **c**, To determine whether the fluorescence observed in PLN was a result of fusion with PLM, or due to a promoter-switching event, time-lapse imaging was undertaken *in vivo*, in *unc-70(s1502)* mutant animals. Single plane images captured on a spinning disk confocal are shown. Asterisk denotes PLM cell body (i); filled arrowhead indicates the site of initial GFP transfer first visible at 0 h (i); open arrowhead indicates site of eventual PLN cell body appearance, which occurs after GFP is visible in the axonal process (ii–ix). Scale bar, 50 μm. Image representative of one fusion event captured from 23 animals imaged. **d**, To further confirm the fusion events in *unc-70(s1502)* mutants, a tethered fluorophore assay was used to analyse cytoplasmic movement between PLM and PLN. Cytoplasmic GFP was expressed together with mRFP targeted to the mitochondria (TOMM-20::mRFP), both expressed under the control of the *Pmec-4* promoter in the same extra-chromosomal array. In wild-type (WT) animals, both GFP and TOMM-20::mRFP are only visible in the soma and axon of the PLM neuron (no extra cell was visible). In those *unc-70(s1502)* mutant animals that presented PLM and PLN spontaneous neuronal fusion visible as GFP in both cells, PLM appeared as per wild-type with TOMM-20::mRFP in the soma and axon (left bar), whereas in PLN (designated 'Extra' in the bar) mitochondria were never observed. Animals with mutations in *sem-4(n1971)* and *ced-3(n717)* contain extra cells due to cell fate defects[35]; as a result, both GFP and TOMM-20::mRFP are visible in the axon and soma of both PLM and the extra cells. Error bars represent standard error of proportion; *n* values for cells analysed in each bar. **e**, Spontaneous fusion between PLM and PLN is completely abolished in *dlk-1* mutants, and shows a large reduction in an *eff-1* mutant background. Overexpression of EFF-1 in the PLM neuron causes a large enhancement in spontaneous fusion events, but in animals lacking DLK-1, overexpression of EFF-1 in PLM is not sufficient to induce neuronal fusion between PLM and PLN. For **d** and **e**, error bars represent standard error of proportion. *n* values are shown adjacent to each bar. *P* values from *t*-test: $***P < 0.001$.

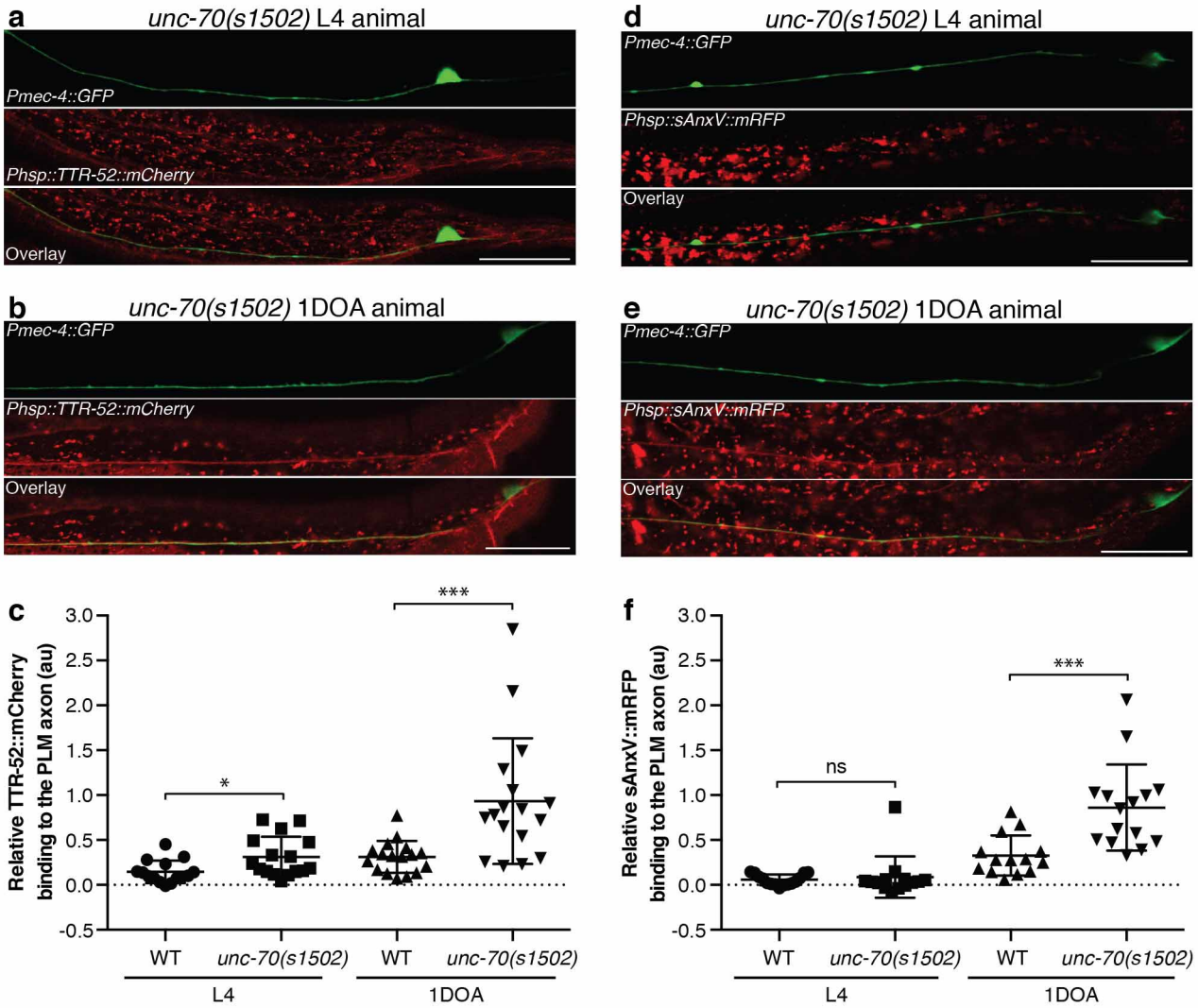

Extended Data Figure 9 | TTR-52 and sAnxV bind to the PLM axon in *unc-70* mutants. Localization of TTR-52::mCherry to the PLM axon at the L4 stage (**a**) or one-day-old adult (1DOA) animal (**b**) of *unc-70* mutant animals (genotype: *unc-70(s1502); oxIs95; smIs119; zdIs5*). Scale bars, 20 µm. Images representative of 16 (**a**) and 17 (**b**) animals. **c**, Quantification of the relative fluorescence levels of TTR-52::mCherry on the PLM axons in L4 and 1DOA wild-type (WT) animals compared to *unc-70(s1502)* mutants. The intensity of TTR-52::mCherry on the axon shows a small but significant increase in *unc-70(s1502)* mutants compared to WT animals at the L4 stage and a more pronounced enhancement in 1DOA animals; $n = 15$ for WT L4, $n = 16$ for *unc-70* L4, and $n = 17$ for both genotypes at 1DOA stage. **d**, Localization of the PS sensor, sAnxV::mRFP, to the PLM axon in an *unc-70(s1502)* mutant animal at the L4 stage. **e**, Localization of sAnxV::mRFP to the PLM axon in a 1DOA *unc-70(s1502)* mutant animal. Scale bars, 20 µm. Images representative of 14 (**d**) and 15 (**e**) animals. **f**, Quantification of the relative fluorescence levels of sAnxV::mRFP on the PLM axons in L4 and 1DOA WT animals compared to *unc-70(s1502)* mutants. In 1DOA animals there is a large increase in the relative fluorescence in *unc-70(s1502)* mutants compared to WT animals; $n = 15$ for WT L4, $n = 14$ for *unc-70* L4, $n = 14$ for WT 1DOA, and 15 for *unc-70* 1DOA. For **c** and **f**, error bars indicate standard error. *P* values from Kolmogorov–Smirnov test: $*P < 0.05$, $***P < 0.001$. ns, not significant. au, arbitrary units.

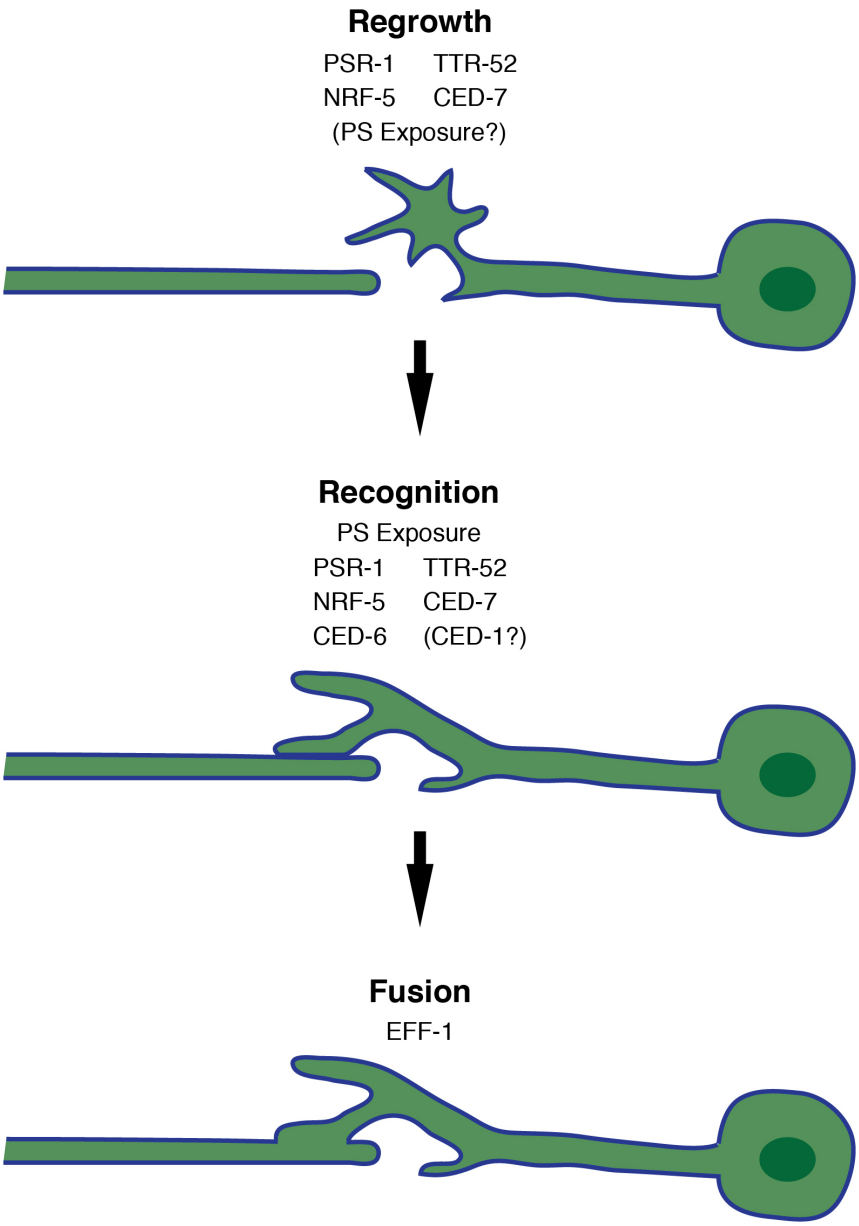

Extended Data Figure 10 | Proposed model for how the apoptotic recognition molecules and the fusogen EFF-1 mediate axonal fusion during regeneration of PLM.